Journal of the Optical Society of Korea
Vol. 20, No. 6, December 2016, pp. 669-677

ISSN: 1226-4776(Print) / ISSN: 2093-6885(Online)
DOI: https://doi.org/10.3807/JOSK.2016.20.6.669

Simulation for Small Lamellar Grating FTIR Spectrometer for Passive Remote Sensing

You Kyoung Chung[1], Choong-Man Jo[1], Seong Kyu Kim[1]*, In Cheol Kim[2], Do-Hyun Park[3], Hyo-Yook Bae[3], and Young Il Kang[4]

[1]*Department of Chemistry and Basic Science Research Institute, Sungkyunkwan University, Suwon 16419, Korea*
[2]*National Institute for Nanomaterials Technology, Pohang 37673, Korea*
[3]*MOORI Technologies, Co., Yongin 17180, Korea*
[4]*The 5th R&D Institute - 3, Agency for Defense Development, Daejeon 34060, Korea*

(Received October 10, 2016 : revised October 25, 2016 : accepted November 8, 2016)

A miniaturized FTIR spectrometer based on lamellar grating interferometry is being developed for passive remote-sensing. Consisting of a pair of micro-mirror arrays, the lamellar grating can be fabricated using MEMS technology. This paper describes a method to compute the optical field in the interferometer to optimize the design parameters of the lamellar grating FTIR spectrometer. The lower limit of the micro-mirror width in the grating is related to the formation of a Talbot image in the near field and is estimated to be about 100 μm for the spectrometer to be used for the wavelength range of 7-14 μm. In calculating the far field at the detection window, the conventional Fraunhofer equation is inadequate for detection distance of our application, misleading the upper limit of the micro-mirror width to avoid interference from higher order diffractions. Instead, the far field is described by the unperturbed plane-wave combined with the boundary diffraction wave. As a result, the interference from the higher order diffractions turns out to be negligible as the micro-mirror width increases. Therefore, the upper limit of the micro-mirror width does not need to be set. Under this scheme, the interferometer patterns and their FT spectra are successfully generated.

Keywords : Lamellar grating, FTIR, Fresnel, Fraunhofer, Boundary diffraction wave
OCIS codes : (050.0050) Diffraction and gratings; (300.0300) Spectroscopy; (260.1960) Diffraction theory; (280.4991) Passive remote sensing; (300.6300) Spectroscopy, Fourier transforms

I. INTRODUCTION

Fourier-transform IR (FTIR) spectroscopy is probably the best optical method for sensing IR radiation from far-away sources. Many FTIR spectrometers for passive remote-sensing are now used in practice or are available on the market. They can easily distinguish radiation from a target chemical and that from the background once the temperature difference in the two radiations is no less than a few degrees [1]. Such high sensitivity in FTIR [2] benefits from multiplex detection (Fellgett's advantage [3]) and high throughput (Jacquinot's advantage [4]) in the interferometry, which are features that are absent in dispersive type spectrometers.

FTIR spectrometers for passive remote-sensing are usually bulky and must be stationed at a fixed location. Such immobility of the spectrometers can be overcome if a small optical element, which may be fabricated by Microelectro-chemical Systems (MEMS) techniques, is substituted for the bulky interferometer part in conventional FTIR spectrometers. Miniaturizing FTIR spectrometers has been an intensive area of research for the past decade. For example, for 3 years beginning in 2008, scientists from companies and research institutes in the European Union worked together in a consortium project called MEMFIS to develop ultrasmall FTIR spectrometers in the mid-IR range [5].

The key element in the ultrasmall spectrometer is either a MEMS mirror or a lamellar grating. Some of those ultrasmall FTIR spectrometers or similar products are now

*Corresponding author: skkim@skku.edu

Color versions of one or more of the figures in this paper are available online.

available on the market. However, extending their applicability to passive remote-sensing still has to wait for further research. In the work detailed in this paper, we were interested in the lamellar grating, which can be created by a MEMS fabrication process, and its potential application for passive remote-sensing in the wavelength region of 7-14 μm (or 700-1400 cm^{-1} in wavenumber). The spectral region of interest is where absorption by water vapor or carbon dioxide is relatively low.

The lamellar grating consists of a pair of mirror arrays. One array is fixed and the other array translates along the direction of incident light. When the reflections from the two mirror arrays are combined at the detector, the detector signal is modulated due to interference induced by the optical path difference (OPD) of the two reflections. The modulation pattern or interferogram is then Fourier-transformed (FT) to give the spectrum of incident light.

The first generation lamellar grating FT spectrometers [6] operated mostly in the far IR region and were very large. Individual mirrors were usually on the order of cm in width, and the overall size of the lamellar grating was on the order of 10 cm. As modern MEMS technology has brought innovative upgrades, lamellar grating FT spectrometers of the second generation were downsized by one or two orders of magnitude. These lamellar grating FT spectrometers have been demonstrated to work at much shorter wavelengths [7-13].

For passive remote-sensing FTIR spectrometers, the MEMS lamellar grating should be as large as possible in order to receive more photons of incident light. This brings up additional difficulties in fabrication, actuation, and optical alignment. The high aspect ratio of individual mirrors in the large MEMS lamellar grating is prone to be bent or twisted in the static state as well as in the dynamic state. For optical alignment, the separation of higher order diffractions from the 0th order (or the reflection) is of great concern as it becomes more difficult to separate undesirable higher order diffractions as the grating size increases.

The performance of the lamellar grating interferometer for the optical part can be simulated by using equations in the scalar diffraction theory, which can be found in most optics textbooks [14, 15]. Based on their simulation, Ferhanoglu *et al*. [11] claimed that the micro-mirror width should be larger than one limit to avoid the Talbot effect [16] and should be smaller than the other limit to separate the ±1st order diffraction. Under this scheme, the micro-mirror width that satisfies both the limits given by the wavelength range and the divergence of incident light is impractical, especially when the grating size is considered. If this is true, all lamellar grating FT spectrometers [7-13], including those [12, 13] designed following their simulation results, must have worked with one of the two handicaps. It was necessary for us to reexamine the equations and simulations to see how seriously the limitations affect the FT spectra for applications in the passive remote-sensing system.

In the following sections, we review the equations in the scalar diffraction theory and their applicability to the passive remote-sensing system. Especially, we found that the Fraunhofer equation is inappropriate to describe the far field at the detection distance of a small-sized lamellar grating interferometer. Then, we introduce an alternative method to describe the far field. The method uses a combination of unperturbed geometry wave and boundary diffraction wave. Using the alternative formalism, higher order diffractions are suppressed to a negligible degree as the mirror width is increased. In the Results section, the analyses from the simulated spectra using the alternative far field equation are shown.

II. METHODS

Figure 1 depicts a one-dimensional (1D) model of the lamellar grating interferometer, which is referenced in this article. In this 1D model, a pair of micro-mirror arrays is patterned along the *x*-axis, while the incident beam, reflected beam, and mirror translation are directed along the *z*-axis. A fixed array of M micro-mirrors whose widths are Δ is placed at $z = 0$. A movable array of M-1 micro-mirrors is then placed at $z = -d$. To comply with the current MEMS fabrication capacity, we will mainly discuss the cases of the overall size (2M-1)×Δ set to about 1 cm and the maximum inter-array distance (d_{max}) set to 500 μm.

2.1. Optical Field in Near-field Zone

The distribution of the optical field in the region close to the grating can be calculated by using equations in the scalar diffraction theory, and we will call this region the 'near field zone'. The Fresnel equation is derived from the paraxial wave theory and is used most frequently. The 1D Fresnel equation is written as follows:

$$\begin{aligned} U(x;d) &= Fr[U(x;0)]_d \\ &= \frac{e^{ikd}}{i\sqrt{\lambda d}}\int U(x';0)\exp\left\{i\frac{k}{2d}(x'-x)^2\right\}dx' \\ &= \frac{e^{ikd}}{i\sqrt{\lambda d}}\exp\left(i\frac{kx^2}{2d}\right)\mathcal{F}\left\{U(x;0)\exp\left(i\frac{kx^2}{2d}\right)\right\} \end{aligned} \quad (1)$$

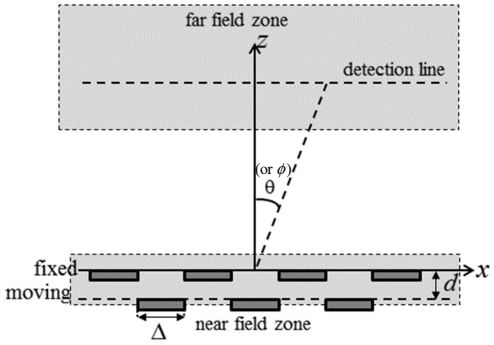

FIG. 1. 1D model of lamellar grating interferometer

Here, $U(x;0)$ is the optical field of source and $U(x;d)$ is the optical field formed at the distance d from the source. k and λ are the wave-vector and wavelength of the light, respectively. $i = \sqrt{-1}$. $Fr[\cdots]_d$ and $\mathcal{F}\{\cdots\}$ denote the Fresnel operator and Fourier-transform operator, respectively.

When $U(x;0)$ is formed by a multi-slit array, the image of the source is reproduced at the so-called Talbot distance d_T [16]: $d_T = \frac{2\Lambda^2}{\lambda} = \frac{8\Delta^2}{\lambda}$, where Λ is the periodicity of the slit array and $\Lambda = 2\Delta$. At the half-Talbot distance $d_T/2$, the phase of $U(x;d_T)$ is completely reversed from that of $U(x;0)$. No light is reflected back if the bottom mirror array is positioned at this distance. Therefore, if d_{max} exceeds $d_T/2$, a node is formed in the interferogram and its FT spectrum displays a satellite peak shifted by $2/d_T$ in wavenumber from the main peak. If d_{max} exceeds d_T, another satellite peak shifted by $1/d_T$ in wavenumber appears in the FT spectrum [11]. The satellite peaks are fairly large and therefore should be avoided by increasing d_T. In order to satisfy $d_{max} < d_T/2$ in the spectral range of interest, the lower limit of the mirror width Δ_{min} is determined as follows:

$$\Delta_{min} = \sqrt{\frac{\lambda_{max} \times d_{max}}{4}} = \sqrt{\frac{14 \times 500\,\mu m^2}{4}} = 42\,\mu m$$

Even when $d_{max} < d_T/2$, the near field meets the Talbot sub-images and a part of the reflecting field leaks out. As a result, the interferogram and the FT spectrum are distorted. To minimize such effects and obtain a uniform near field, $d_T/2$ should be farther away from d_{max}, which pushes the practical lower limit of Δ further to a higher value.

The optical field at the grating facet at $z = 0$, $U_0(x;d)$, is composed of reflections from the top mirror array and from the bottom mirror array:

$$U_0(x;d) = U_1(x;0) + U_2(x;d) \tag{2}$$

Under the initial condition that $U_1(x;0) + U_2(x;0) = 1$ for all x,

$$U_0(x;d) = (1 - T(x)) - T(x)Fr[T(x)Fr[T(x)]_d]_d \tag{3}$$

where $T(x)$ is a transmission function of the mirror array; 1 for x in the open region and 0 for x in the reflection region. The first term in the right side of Eq. (2) or (3) represents the field remaining on the top array, while the second term represents the field that is transmitted through the top array followed by being reflected by the bottom array.

2.2. Fraunhofer Approximation to Describe the Far Field

The optical field generated in the near field zone, $U_0(x;d)$, propagates outward, and part of it is collected by a detection window set at some distance away. We call the area around the detection window the 'far field zone'. The detection window may represent an optical component with which the 0th order diffraction is picked off and redirected into a detector. To collect most of the 0th order diffraction, the size of the detection window is recommended to be slightly larger than the overall size of the grating. The location of the detection window should be determined for alignment convenience but must be no greater than about 15 cm since the overall size of the spectrometer should not be large.

Under the condition that the incident light is normally directed toward the grating with unit amplitude and equal phase, the optical field formed at the grating facet ($z = 0$) can be described without going into much detail in the near field as follows:

$$\begin{aligned} U_0(x;d) = &\sum_{m=-M/2+1}^{M/2} rect(x - 2m\Delta + \Delta) \\ &+ \sum_{m=-M/2+1}^{M/2-1} rect(x - 2m\Delta)\exp(-4\pi i d/\lambda) \end{aligned} \tag{4}$$

where $rect(\cdots)$ represents the rectangular function. The second term represents the field on the movable array, which has the phase term given by the OPD of $2d$ relative to the fixed array described in the first term. The analytical expression for the far field generated from the above $U_0(x;d)$ can be obtained under the Fraunhofer approximation. Following the work of Strong and Vanasse [6], the intensity of light diffracted into angle ϕ can be given by

$$I(\phi;d) = \left(\frac{\sin X}{X}\right)^2 \left(\frac{\sin 2MX}{\sin 2X}\right)^2 \cos^2\left(\frac{2\pi d}{\lambda} + \frac{X}{2}\right) \tag{5}$$

where $X = \pi\Delta\sin\phi/\lambda$. The first factor on the right side of Eq. (5) describes the field intensity produced by a single micro-mirror, while the second factor describes the combined field intensity produced by all micro-mirrors. The third factor is a phase factor.

The second factor reaches relative maxima when the denominator goes to zero: $2X = m\pi$. This provides the condition for m-th order diffraction:

$$2\Delta\sin\phi_m = m\lambda,\ m = 0, \pm1, \pm2, \ldots \tag{6}$$

When m is an even number other than zero, the first factor is zero. Therefore, the diffracted light is mostly focused in directions of the 0th order and a few odd orders. The third factor determines the OPD for the relative maxima of a given diffraction order. The intensity of the 0th order reaches a relative maximum when d is an even multiple of $\lambda/4$ and a relative minimum when d is an odd multiple of $\lambda/4$. On the other hand, the intensity of odd orders is a relative

maximum when d is an odd multiple of $\lambda/2$ and a relative minimum when d is an even multiple of $\lambda/2$. In other words, the 0th order diffraction is out of phase with the odd order diffractions.

The relative maximum of the m-th order diffraction is determined by the first factor of Eq. (5). The ratio of relative maxima for the 0th order and the 1st order diffractions is 1: $\mathrm{sinc}^2(\pi/2)$ or $1{:}4/\pi^2$. Therefore, the overall contribution of the ±1st orders amounts to 81% of the 0th order. This amount of ±1st order contribution is not insignificant. If the ±1st orders are fully mixed with the 0th order in the detection window, the modulation in the interferogram is reduced by 5 times. This raises the first question regarding the validity of the Fraunhofer approximation for our application. The diffraction of plane-wave should be less important as Δ/λ increases. However, such a consideration is not fulfilled in Eq. (5), in which the contribution of the odd order diffractions is independent of Δ/λ. This raises the second question regarding the Fraunhofer approximation.

In an alternative manner, the near field can be obtained numerically using Eqs. (1)-(3). Then, the numerically obtained $U_0(x;d)$ can be used to find the numerical solution for the far field $U_z(x;d)$. Here again, the 1D Fraunhofer equation can be used:

$$U_z(x;d) = \frac{1}{\sqrt{i\lambda z}} \int U_0(x';d) \exp(-ikxx'/z)dx' \tag{7}$$

If the incident light is off-normal to the grating by θ, we replace d by $d/\cos\theta$ to reflect the phase difference in the near field and x/z by $\tan\{\tan^{-1}(x/z)+\theta\}$ to reflect the direction change in the far field.

$$U_{z,\theta}(x;d) = \frac{1}{\sqrt{i\lambda z}} \int U_0(x';d/\cos\theta) \times \exp\left[-ikx' \cdot \tan\{\tan^{-1}(x/z)+\theta\}\right]dx' \tag{8}$$

where $\tan^{-1}$ represents arctangent.

When the incident light has the half-divergence $\delta\theta$, the far field intensity is obtained as follows:

$$I_z(x;d) = \int_{-\delta\theta}^{\delta\theta} w(\theta) \left|U_{z,\theta}(x;d)\right|^2 d\theta \tag{9}$$

where $w(\theta)$ is a weighing factor. As a matter of fact, Eqs. (1)-(3) and (7)-(9) must be the same as those used by Ferhanoglu *et al*. [11]. Using these equations, we are able to reproduce successfully their interferograms and the FT spectra.

To examine the validity of the Fraunhofer equations, the far field intensity distribution is calculated and presented in Fig. 2. The inter-array distances were dually set to $\lambda/2$ and $3\lambda/4$ to produce the relative maxima for the 0th order and the ±1st order diffractions, respectively. The intensities

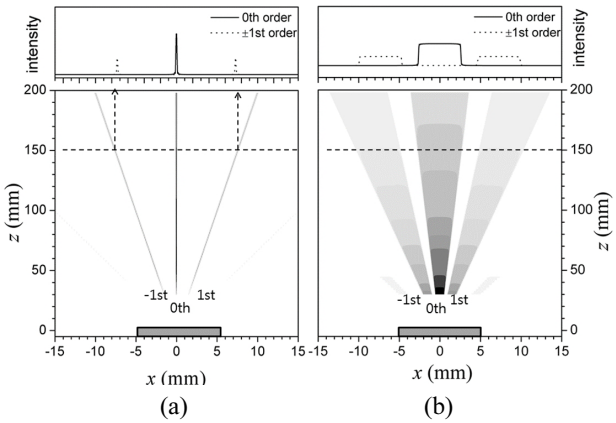

FIG. 2. The far field intensity distribution calculated with the Fraunhofer equation; (a) when $\delta\theta = 0°$ and (b) when $\delta\theta = 1.0°$. The other common parameters: $\lambda = 10$ μm, $\Delta = 100$ μm, $M = 50$. In ease case, the bottom gray-scaled plot is produced by overlapping the field intensities at $d = \lambda/2$ (for the 0th order maximum) and at $d = 3\lambda/4$ (for the ±1st order maximum). The top plots show the cross-section of the bottom plots at $z = 150$ mm. The gray block of 1 cm length in the bottom plots represents the lamellar grating.

from the two inter-array distances are then overlapped in the bottom gray-scaled plots. Their cross-sections at z = 150 mm are shown in the top plots. Figure 2(a) is the case when the incident light has no divergence. The 0th order diffraction, formed along the center line of the grating, is sharply distributed across x; the FWHM of the cross-section is approximately 50 μm. The ±1st order diffractions are also distributed sharply across x. The simplified expression of far field in Eq. (5) would show the similar plots.

Figure 2(b) is the case when the incident light has a half-divergence ($\delta\theta$) of 1.0°. The directions of both the 0th order and the ±1st orders are dispersed by $2\delta\theta$ or 2.0°. When this dispersion is greater than the diffraction angle of the 1st orders, $\sin^{-1}(\lambda/2\Delta)$, the ±1st orders overlap with the 0th order, and reduce the interferogram modulation. Ferhanoglu *et al*. [11] tried to find the upper limit of the micro-mirror width to avoid the overlap; that is, $\Delta_{max} = \lambda_{min}/\{2\sin(2\delta\theta)\}$. When λ_{min} = 7 μm and $\delta\theta$ = 1.0°, Δ_{max} is found to be 100 μm. This estimation, however, does not consider the overall size of the grating. The larger the size of the grating, the more tightly imposed the width limit or the divergence limit should be. Actually, with a size of 1 cm for our passive remote-sensing application, it is not possible to discriminate the ±1st orders if the detection window is placed less than 15 cm from the grating.

In spite of the negative speculations on the lamellar grating, we find that Fig. 2 does not demonstrate our expectations that the far field should reflect the image of the grating. In addition, as mentioned previously, the relative intensities of the ±1st orders remain invariant when Δ or λ is varied. This implies that using the Fraunhofer approximation is inappropriate for our application. In formulating the Fraunhofer

equation, the light source is assumed to be coherently generated from a single far-away point located on the x = 0 axis. Considering that the Fraunhofer equation is a plane-wave approximation of the Fresnel equation, superimposing plane-waves naturally into the x = 0 axis requires a very long z, which is not within the range of our application.

2.3. Boundary Diffraction Wave to Describe the Far Field

In the scalar diffraction theories following Huygens and Kirchhoff, the light passing through a hole is described by a surface integral of the spherical waves originating from the hole. In the alternative boundary diffraction wave (BDW) approach, Maggi [17] and Rubinowicz [18] independently showed that the problem is equivalent to solving a line integral for the spherical waves generated at the hole boundary in addition to the geometry wave that passes through the hole without perturbation. This postulate was further developed by many scientists and applied to numerous problems such as plane wave propagation over a knife-edge or through a slit [20-27].

When the BDW approach is applied to our problem, the far-field $U_{z,\theta}(x;d)$ is given as follows:

$$U_{z,\theta}(x;d) = U_0(x';d/\cos\theta)\exp(ikz/\cos\theta) + \sum_E U_E(x';d/\cos\theta) \qquad (10)$$
$$x' = x - z\tan\theta$$

where the first term on the right hand side of Eq. (10) represents the propagation of the unperturbed plane-wave and the second term is for the BDW, where E represents the edge points of all micro-mirrors.

The formulations for the BDW in 1D slit-like problems are found in a few references [19-21]. Following Keller's derivation [19],

$$U_E(x';d/\cos\theta) = \pm\frac{e^{i\pi/4}}{4\pi}\sqrt{\frac{\lambda}{r}}\exp(-ikr)\times\{\sec(\pi-\phi)/2 + \csc(\pi-\phi)/2\}\times U_0(x_E;d/\cos\theta) \qquad (11)$$

where $r = \sqrt{z^2\cos^2\theta + (x'-x_E)^2}$ and x_E is the coordinate of the edge points. Edge points are set at the leftmost and rightmost coordinates of each micro-mirror. The positive sign in Eq. (11) is assigned to the left edge and the negative sign is assigned to the right edge, or vice versa, in order to satisfy the boundary condition.

Examples of the far field calculated with Eqs. (10), (11) are shown in Fig. 3. Fig. 3(a) is the case when $d = \lambda/2$, where almost no BDW appears as they are cancelled by contributions from neighboring edge points (one for the right edge of n-th mirror and the other for the left edge of the (n+1)-th mirror) with opposite phases. The unperturbed plane-wave dominates the far field in this case. Figure 3(b) is the case when $d = 3\lambda/4$. The BDW appears in the

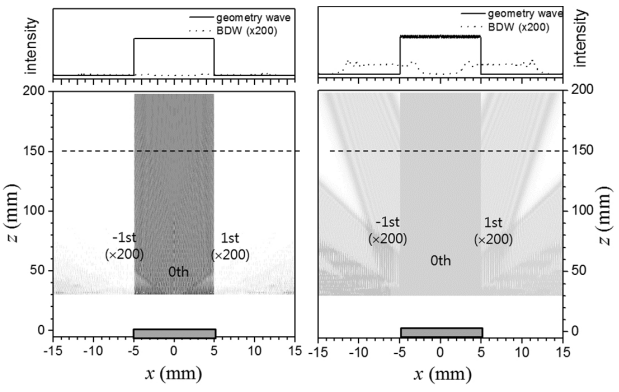

FIG. 3. Optical field intensity distribution when the far field is given by the unperturbed plane-wave and the BDW; (a) when $d = \lambda/2$, (b) when $d = 3\lambda/4$. The other common parameters: $\lambda = 10$ μm, $\Delta = 100$ μm, M = 50, $\delta\theta = 0°$. The field intensity from the BDW was multiplied by 200 times in order to be shown on the same plot as the unperturbed plane wave. On the top, the cross section at z = 150 mm is shown.

directions of ±1st and ±3rd order diffractions and is absent in the direction of the 0th order. The intensities of the higher order diffractions are very small compared to that of the 0th order. Take notice that Fig. 3(b) is produced by multiplying the intensity of the BDW by 200 times in order to be plotted together with the unperturbed plane-wave. The sum of the ±1st order intensities amounts to only 0.4% of the 0th order intensity. Under this condition, the ±1st order diffractions do not need to be separated as the interferogram is produced exclusively by the plane-wave reflected with little perturbation, or the 0th order diffraction.

When Δ is increased while the overall size of the grating is fixed, the number of edge points decreases. It decreases the contribution of the BDW in the detected intensity. In addition, the BDW intensity is proportional to λ as is implied in Eq. (11). Overall, the BDW intensity or contribution of the high order diffractions is inversely proportional to Δ/λ.

2.4. The Interferogram and Spectrum

To obtain an interferogram, the far field is integrated over the detection window. The integrated field as a function of the OPD (= 2d) is the interferogram:

$$I(D) = \frac{1}{(2M-1)\Delta}\int_{\lambda_{min}}^{\lambda_{max}} s(\lambda)\int_{-\delta\theta}^{\delta\theta} w(\theta)\left|\int_{det} U_{z_{det},\theta}(x;D/2)dx\right|^2 d\theta d\lambda \qquad (12)$$

where D = 2d. The innermost integration is over the detection window at $z = z_{det}$, and the integrations over θ and λ are to consider the beam divergence and the spectral range of interest, respectively. As normalized functions for the angular weight $w(\theta)$ and the spectrum $s(\lambda)$ are used

and no unit is given to any fields U, $I(D)$ should have the dimension of length.

The interferogram is then Fourier-transformed to give the spectrum:

$$S(\bar{\nu}) = \mathcal{F}^{-1}\{I(D)\} \tag{13}$$

where $\mathcal{F}^{-1}\{...\}$ is the inverse Fourier-transform operator and $\bar{\nu}$ $(= 1/\lambda)$ is the wavenumber.

III. RESULTS

The equations that we have presented in previous sections were written in a FORTRAN code to compute the optical field distribution, interferogram, and spectrum under numerous conditions. The codes also include the following features that are not detailed in this paper: the phase correction, the apodization, the zero-filling, the effect of additional gap between neighboring micro-mirrors, etc. (Minimum gap size is given by the distance between two sampling points at x = 0, and additional gaps are created by nullifying the source field at edge points of each micro-mirror.) A couple of the computed interferograms and spectra are illustrated in Fig. 4. This is the case when the incident light has a single wavelength: $s(\lambda) = \delta(\lambda-\lambda_0)$ and λ_0 = 10.4987 μm. The major difference in the two sets of computation parameters is the micro-mirror width; it is 100 μm for Fig. 4(a1) and 4(a2) while it is 500 μm for Fig. 4(b1) and 4(b2). The overall sizes of the grating (2M-1)Δ are very close; they are 0.99 cm and 0.95 cm, respectively, which are reflected in the values of $I(0)$ in Fig. 4(a1) and 4(b1). All the other computation parameters are identical in the two sets.

The interferogram for Δ = 500 μm is covered with a more uniform envelope than that for Δ = 100 μm, as the Talbot image of the former case is farther away from d_{max}. Accordingly, the FT spectra of the two cases are slightly different. The spectral points are computed with an interval of $1/(4d_{max})$, or 5 cm^{-1} in this case, and their intensities are peaked near $1/\lambda_0$, or 952.5 cm^{-1} in this case.

To evaluate the spectra in more detail, a following reference function is plotted together in Fig. 4(a2) and 4(b2):

$$S_{ref}(\bar{\nu}) = A\,\mathrm{sinc}\left(4\pi(\bar{\nu} - 1/\lambda_0)d_{\max}\right) \tag{14}$$

The amplitude A is determined to give a minimum (root mean square) error between the computed and the reference spectra:

$$err = \sqrt{\frac{1}{n}\sum_{i=1}^{n}\left(\hat{S}(\bar{\nu}_i) - S_{ref}(\bar{\nu}_i)\right)^2} \times 100\,(\%) \tag{15}$$

where $\hat{S}(\bar{\nu}_i)$ is the computed spectral intensity divided by its peak value and n is the number of computed spectral

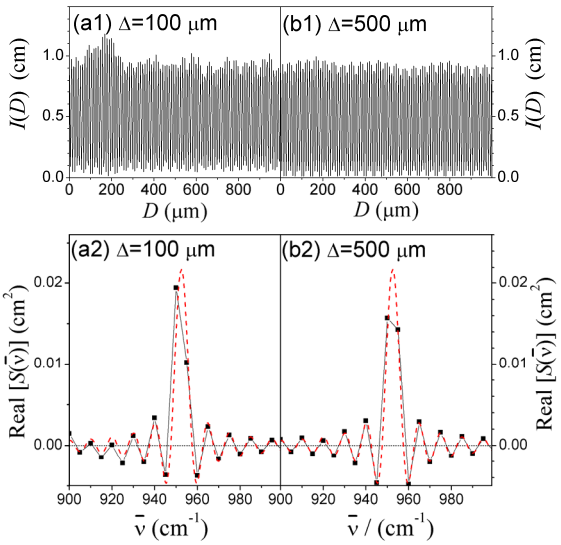

FIG. 4. Examples of the interferogram and spectrum. (a1) and (a2) were obtained with Δ = 100 μm and M = 50 while (b1) and (b2) were obtained with Δ = 500 μm and M = 10. The other computation parameters are identical; λ_0 = 10.4987 μm, δθ = 0°, detector size = 1.2 cm, z_{det} = 10 cm, and no additional gap between neighboring micro-mirrors is placed. The interferograms are shown only in the positive side of D, and the real parts of the spectrum are shown. In the spectra, the computed points are shown with filled squares, while red dashed curves represent the best fit sinc function.

points in the fit range. The sinc function in Eq. (14) is a Fourier-transform of a boxcar function, and should be an ideal spectral response of the single wavelength input. When the simple expression of the near field in Eq. (4) is used instead of Eqs. (1)-(3), the computed spectral intensities follow almost exactly the $S_{ref}(\bar{\nu})$ in Eq. (14). This implies that the difference in the two spectra in Fig. 4 is mainly due to the near field details. The error values for the two computed spectra in Fig. 4 are 6.3% for Δ = 100 μm and 1.1% for Δ = 500 μm, respectively. Apparently, the smaller error with the larger Δ is related to the interferogram being covered with a more uniform envelope.

The *err* values as the wavelength, the half-divergence, and the size of the gap between neighboring micro-mirrors are varied are tabulated in Table 1. (Take notice that the wavelengths in Table 1 as well as in Fig. 4 are chosen in such a way that $1/\lambda_0$ is a mid-wavenumber of two neighboring points in the FT spectrum. Otherwise, an asymmetric positioning of sinc function with respect to the FT spectrum may produce an artifact in *err* values.). The *err* value increases when the wavelength or the gap size increases as the uniformity in the interferogram envelope decreases. However, the *err* value decreases first as δθ increases and then it turns around to increases as δθ increases further. This trend can be understood as follows. Figure 4 shows that the non-uniformity in the interferogram envelope enhances the low frequency component. However, increasing off-normal incident angle

TABLE 1. Error values (*err*) of the computed spectra for single wavelength inputs. M=50 when Δ=100 μm and M=10 when Δ=500 μm

λ_0 (μm)	Δ (μm)	δθ	gap (μm)	*err* (%)	λ_0 (μm)	Δ (μm)	δθ	gap (μm)	*err* (%)	λ_0 (μm)	Δ (μm)	δθ	gap (μm)	*err* (%)
7.02987	100	0°	5	0.9	10.4987	100	0°	5	6.3	13.9373	100	0°	5	7.5
7.02987	100	0°	10	0.9	10.4987	100	0°	10	6.9	13.9373	100	0°	10	8.3
7.02987	100	0°	15	0.9	10.4987	100	0°	15	7.3	13.9373	100	0°	15	9.0
7.02987	100	0°	20	0.9	10.4987	100	0°	20	8.1	13.9373	100	0°	20	10.2
7.02987	100	0.5°	5	0.7	10.4987	100	0.5°	10	6.2	13.9373	100	0.5°	5	7.5
7.02987	100	1.0°	5	0.3	10.4987	100	1.0°	15	5.8	13.9373	100	1.0°	5	7.2
7.02987	100	1.5°	5	1.1	10.4987	100	1.5°	5	5.2	13.9373	100	1.5°	5	6.8
7.02987	100	2.0°	5	2.4	10.4987	100	2.0°	5	4.4	13.9373	100	2.0°	5	6.2
7.02987	100	2.5°	5	4.2	10.4987	100	2.5°	5	3.4	13.9373	100	2.5°	5	5.3
7.02987	100	3.0°	5	6.2	10.4987	100	3.0°	5	2.4	13.9373	100	3.0°	5	4.4
7.02987	100	4.0°	5	10.8	10.4987	100	4.0°	5	5.0	13.9373	100	4.0°	5	2.6
7.02987	500	0°	5	0.9	10.4987	500	0°	5	1.1	13.9373	500	0°	5	1.3
7.02987	500	0°	10	0.9	10.4987	500	0°	10	1.2	13.9373	500	0°	10	1.4
7.02987	500	0°	15	0.9	10.4987	500	0°	15	1.2	13.9373	500	0°	15	1.4
7.02987	500	0°	20	0.9	10.4987	500	0°	20	1.2	13.9373	500	0°	20	1.4
7.02987	500	0.5°	5	0.7	10.4987	500	0.5°	5	1.0	13.9373	500	0.5°	5	1.2
7.02987	500	1.0°	5	0.3	10.4987	500	1.0°	5	0.6	13.9373	500	1.0°	5	0.9
7.02987	500	1.5°	5	1.1	10.4987	500	1.5°	5	0.5	13.9373	500	1.5°	5	0.5
7.02987	500	2.0°	5	2.4	10.4987	500	2.0°	5	1.2	13.9373	500	2.0°	5	0.6
7.02987	500	2.5°	5	4.2	10.4987	500	2.5°	5	2.4	13.9373	500	2.5°	5	1.4
7.02987	500	3.0°	5	6.2	10.4987	500	3.0°	5	4.4	13.9373	500	3.0°	5	2.5
7.02987	500	4.0°	5	10.8	10.4987	500	4.0°	5	7.2	13.9373	500	4.0°	5	5.2

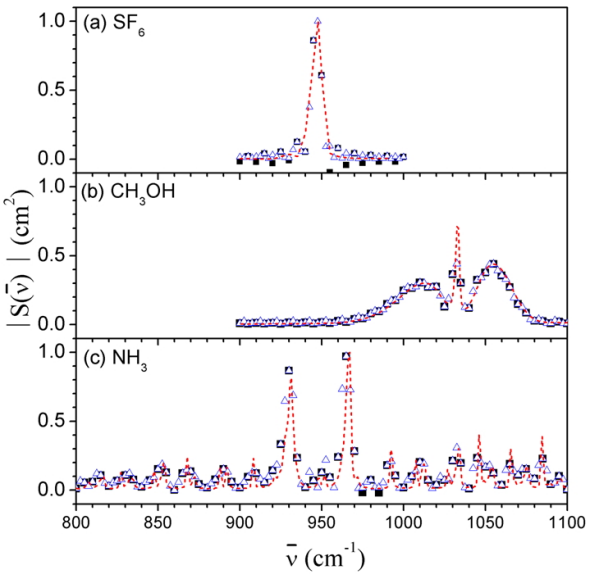

FIG. 5. Computed spectra of SF_6 (a), CH_3OH (b), and NH_3 (c). The red dashed curves are the reference spectra. The black filled squares are the spectral points calculated with no zero filling while the blue open triangles are the points calculated with the zero filling. Common computation parameters of these plots: Δ =100 μm, M=50, δθ = 0°, no additional gap between micro-mirrors.

works in the opposite direction. This is because the phase advance by (1/cosθ -1)×OPD increases the high frequency component. The FT spectrum becomes more symmetric and *err* value decreases as δθ increases from 0° to a certain turning point due to the compensation of the two effects. As δθ increases further from the turning point, the FT spectrum becomes asymmetric with more intensity in the high frequency side as the phase advance effect is dominant.

The FT spectra calculated with a few gas spectra as the inputs are illustrated in Fig. 5 and the *err* values under numerous conditions are listed in Table 2. As the interval of the spectral points is 5 cm^{-1} (= $1/4d_{max}$), the sharp peaks in the CH_3OH spectrum or NH_3 spectrum are not clearly resolved. This may be improved by padding extra zeros outside the OPD maximum in the interferogram. While the zero-filling helps to expose the sharp peaks, it slightly deteriorates broad features. The zero-filling over twice the OPD maximum does not improve the spectral matching any more.

IV. DISCUSSION

As length in optical problems is scaled with the wavelength of light, features in lamellar grating interferometry are preserved when Δ/λ is constant. Table 3 compares the working wavelength range, Δ, and Δ/λ for a few lamellar grating FT spectrometers developed so far. Especially intriguing to the current discussion is Δ/λ_{min}, which is denoted with bold numbers in Table 3. The spectrometer of reference 13 was developed under the MEMFIS project of the European Union. The design parameters for this spectrometer were

TABLE 2. Error values (*err*) of the computed spectra for spectrum inputs. The *err* values calculated with the zero-filling are shown in square brackets. For the gap size, the minimum (5 μm) corresponds to the distance between two neighboring sampling points at x=0

spectrum	Δ (μm)	δθ	gap (μm)	*err* (%)	spectrum	Δ (μm)	δθ	gap (μm)	*err* (%)	spectrum	Δ (μm)	δθ	gap (μm)	*err* (%)
SF_6	100	0°	5	7.8[4.3]	CH_3OH	100	0°	5	6.0[4.6]	NH_3	100	0°	5	8.0[8.0]
SF_6	100	0°	10	7.8[4.2]	CH_3OH	100	0°	10	6.2[4.7]	NH_3	100	0°	10	8.1[8.2]
SF_6	100	0°	15	7.9[4.3]	CH_3OH	100	0°	15	6.2[4.7]	NH_3	100	0°	15	8.1[7.3]
SF_6	100	0°	20	7.9[4.3]	CH_3OH	100	0°	20	6.4[4.9]	NH_3	100	0°	20	8.3[8.5]
SF_6	100	0.5°	5	8.0[4.3]	CH_3OH	100	0.5°	5	5.9[4.6]	NH_3	100	0.5°	5	8.0[8.0]
SF_6	100	1.0°	5	8.0[4.4]	CH_3OH	100	1.0°	5	5.8[4.5]	NH_3	100	1.0°	5	8.0[7.9]
SF_6	100	1.5°	5	7.9[4.5]	CH_3OH	100	1.5°	5	5.7[4.5]	NH_3	100	1.5°	5	8.0[7.9]
SF_6	100	2.0°	5	7.9[4.7]	CH_3OH	100	2.0°	5	5.5[4.4]	NH_3	100	2.0°	5	8.1[7.7]
SF_6	100	2.5°	5	7.9[5.0]	CH_3OH	100	2.5°	5	5.2[4.3]	NH_3	100	2.5°	5	8.1[7.6]
SF_6	100	3.0°	5	8.0[5.4]	CH_3OH	100	3.0°	5	4.8[4.3]	NH_3	100	3.0°	5	8.3[7.6]
SF_6	100	4.0°	5	8.5[6.8]	CH_3OH	100	4.0°	5	3.6[4.4]	NH_3	100	4.0°	5	9.0[7.6]
SF_6	500	0°	5	9.3[6.2]	CH_3OH	500	0°	5	5.3[4.1]	NH_3	500	0°	5	8.1[7.3]
SF_6	500	0°	10	9.1[6.1]	CH_3OH	500	0°	10	5.3[4.1]	NH_3	500	0°	10	8.1[7.3]
SF_6	500	0°	15	9.3[6.2]	CH_3OH	500	0°	15	5.3[4.1]	NH_3	500	0°	15	8.1[7.3]
SF_6	500	0°	20	9.3[6.2]	CH_3OH	500	0°	20	5.3[4.1]	NH_3	500	0°	20	8.1[7.3]
SF_6	500	0.5°	5	9.2[6.2]	CH_3OH	500	0.5°	5	5.3[4.1]	NH_3	500	0.5°	5	8.1[7.3]
SF_6	500	1.0°	5	9.4[6.3]	CH_3OH	500	1.0°	5	5.2[4.1]	NH_3	500	1.0°	5	8.2[7.3]
SF_6	500	1.5°	5	9.5[6.6]	CH_3OH	500	1.5°	5	5.1[4.1]	NH_3	500	1.5°	5	8.3[7.2]
SF_6	500	2.0°	5	9.7[7.0]	CH_3OH	500	2.0°	5	4.9[4.1]	NH_3	500	2.0°	5	8.5[7.3]
SF_6	500	2.5°	5	10.1[7.5]	CH_3OH	500	2.5°	5	4.7[4.1]	NH_3	500	2.5°	5	8.8[7.3]
SF_6	500	3.0°	5	10.5[8.3]	CH_3OH	500	3.0°	5	4.4[4.2]	NH_3	500	3.0°	5	9.1[7.4]
SF_6	500	4.0°	5	11.7[10.0]	CH_3OH	500	4.0°	5	4.0[4.6]	NH_3	500	4.0°	5	10.1[8.0]

TABLE 3. Length parameters of lamellar grating spectrometers demonstrated so far. Δ/λ_{min} values are in bold

λ range	Δ	Δ/λ	reference
2.5-16 μm	65 μm	4-**26**	13
9-4000 μm	6.4 mm	1.6-**700**	6
0.4-0.8 μm	45 μm	56-**113**	7
0.3-1.0 μm	10 μm	10-**33**	8

based on the work of Ferhanoglu *et al*. [11]. Since they imposed the upper limit to Δ to separate the higher order diffractions, Δ/λ_{min} is too small for comparison with others. In contrast, Δ/λ_{min} values for the first generation spectrometer made by Strong and Vanasse [6] as well as the second generation spectrometer made by Manzardo *et al*. [7] are at least 5 times greater. With the Δ/λ values, the higher order diffractions cannot be separated; yet, they demonstrated that the spectrometers worked all right. This implies that the contribution of higher order diffractions is negligible and the Fraunhofer approximation that leads to significant contribution of higher order diffraction was used incorrectly in the development of MEMFIS lamellar grating spectrometers.

When the higher order diffractions are neglected, the interferogram and its FT spectrum are characterized by the unperturbed plane-wave in the far field. Under such an ideal condition, the spectral resolution is determined by the maximum OPD or $2d_{max}$. However, the unperturbed plane-wave is in fact perturbed in the near field even if d_{max} is shorter than $d_\Gamma/2$. This brings about slight distortion in the interferogram. Such an undesirable feature can be minimized as Δ is increased to give larger d_Γ. Increasing Δ would also be desirable since a larger d_{max} can be utilized, resulting in better spectral resolution,

When the criteria of spectral resolution ($\Delta\bar{\nu}$) is that two peaks are distinguishable with a dip larger than 20% of the peak intensity, $\Delta\bar{\nu} = 0.73/(2d_{max})$ or 7.3 cm^{-1} in our case. (See Chapter 2 of Reference 2.) This is the best spectral resolution that can be achieved with the maximum inter-array distance of 500 μm. The deviation from the ideal spectral shape as we represented with the *err* values would deteriorate the spectral resolution. If the input parameters are limited to comply with our application ($\Delta \geq 100$ μm, $7 \leq \lambda_0 \leq 14$ μm, $\delta\theta \leq 2.5^o$, the gap size $\leq$ 15 μm), the maximum *err* value in Table 1 is 9.0%. This much error is small enough to ensure the spectral resolution within 10 cm^{-1}.

In our method of calculation, all the reflections from the micro-mirrors are assumed to be combined at one point. This necessitates a setup of optical elements at the detection window in order to pick up and focus the field into a single point at a detector. In practice, the field is focused into a diffraction-limited spot rather than into a single point, and aberrations in the focusing optics and divergence in the reflected beam broadens the focused spot. Such practical and

non-ideal situations are likely more tolerable with smaller Δ's. Therefore, even if the upper limit of Δ is not necessarily imposed to separate higher order diffractions, there must be an upper limit of Δ under practical condition of optical setup.

V. CONCLUSION

In this paper, we considered the design parameters for a miniature lamellar grating FTIR spectrometer to be used for passive remote-sensing. Especially, the width of micro-mirrors is of concern. It should be greater than about 100 μm to minimize the Talbot effects in the near field. Previously, an upper limit was imposed to separate higher order diffractions from the 0th order in the far field. The upper limit does not appear to be met for the remote-sensing applications. However, the upper limit was based on a misguided Fraunhofer equation used to describe the far field. We instead used a BDW approach and showed that the contribution of the higher order diffractions is negligible when the micro-mirror width is greater than 100 μm. The performance of the spectrometer is mainly determined by unperturbed reflections and near field details. The upper limit of the micro-mirror is not necessarily set in order to avoid higher order diffractions but may be set by other practical reasons such as the efficiency of collecting reflections off a wide area of lamellar grating and focusing them into a small detector area. The development of a miniature lamellar grating FTIR spectrometer is on-going under these guidelines.

ACKNOWLEDGMENT

This work was carried out with the support of the Chemical and Biological Detection Research Center (CBD32). YKC was also supported by the Program for Returners into R&D (KW- 2015-PPD-0175) of Center for Women in Science, Engineering and Technology.

REFERENCES

1. R. Harig, "Passive remote sensing of pollutant clouds by Fourier-transform infrared spectrometry: signal-to-noise ratio as a function of spectral resolution," Appl. Opt. **43**, 4603-4610 (2004).
2. P. R. Griffiths and J. A. de Haseth, *Fourier Transform Infrared Spectroscopy*, 2nd ed., (John Wiley & Sons, Inc., New York, NY, USA, 2007).
3. P. B. Fellgett, "On the ultimate sensitivity and practical performance of radiation detectors," J. Opt. Soc. Am. **39**, 970-979 (1949).
4. P. Jacquinot, "New developments in interference spectroscopy," Rep. Prog. Phys. **23**, 267-312 (1960).
5. Refer the following web pages: https://www.technikon.com/projects/former/memfis, http://home.ku.edu.tr/~mems/memfisproject.html, http://cordis.europa.eu/project/rcn/86631_en.html.
6. J. Strong and G. A. Vanasse, "Lamellar grating far-infrared interferometer," J. Opt. Soc. Am. **50**, 113-118 (1960).
7. O. Manzardo, R. Michaely, F. Schädelin, W. Noell, T. Overstolz, N. D. Rooij, and H. P. Herzig, "Miniature lamellar grating interferometer based on silicon technology," Opt. Lett. **29**, 1437-1439 (2004).
8. Y. Hongbin, Z. Guangya, C. F. Siong, L. Feiwen, W. Shouhua, and Z. Mingsheng, "An electromagnetically driven lamellar grating based Fourier transform microspectrometer," Micromech. Microeng. **18**, 055016 (2008).
9. W. Shouhua, Y. Hongbin, and C. F. Siong, "A miniaturized lamellar grating based Fourier transform spectrometer with electrostatic actuation," IEEE Sensors J. **10**, 1869-1874 (2010).
10. C. Ataman, H. Urey, and A. Wolter, "A Fourier transform spectrometer using resonant vertical comb actuators," J. Micromech. Microeng. **16**, 2517-2523 (2006).
11. O. Ferhanoglu, H. R. Seren, S. Lüttjohann, and H. Urey, "Lamellar grating optimization for miniaturized fourier transform spectrometers," Opt. Express **17**, 21289-21301 (2009).
12. H. R. Seren, S. Holmstrom, N. P. Ayerden, J. Sharma, and H. Urey, "Lamellar-grating-based MEMS fourier transform spectrometer," J. Microelectrochem. Sys. **21**, 331-339 (2012).
13. N. P. Ayerden, U. Aygun, S. T. S. Holmstrom, S. Olcer, B. Can, J.-L. Stehle, and H. Urey, "High-speed broadband FTIR system using MEMS," Appl. Opt. **53**, 7267-7272 (2014).
14. J. W. Goodman, *Introduction to Fourier Optics*, 3rd ed. (Roberts & Company Publishers, Englewood, CO, USA, 2005).
15. M. Born and E. Wolf, *Principles of Optics*, 7th ed. (Cambridge University Press, Cambridge, UK, 1999).
16. H. F. Talbot, "Facts relating to optical science No. IV," Philos. Mag. Ser. III, **9**, No. 56 (1836).
17. G. A. Maggi, "Sulla propagazione libera e perturbata delle onde luminose in mezzo isotropo," Ann. di Math. IIa **16**, 21-48 (1888).
18. A. Rubinowicz, "Die Beugungswelle in der Kirchhoffschen Theorie der Beugungserscheinungen," Ann. Physik, **53**, 257-278 (1917).
19. J. B. Keller, "Geometrical theory of diffraction," J. Opt. Soc. Am. **52**, 116-130 (1962).
20. S. Ganci, "Boundary diffraction wave theory of Rubinowicz for rectilinear apertures," Eur. J. Phys **18**. 229-236 (1997).
21. U. Yalçin, "Uniform scattered fields of the extended theory of boundary diffraction wave for PEC surfaces," Prog. Electromag. Res. **7**, 29-39 (2009).
22. S. Wang, "On principles of diffraction," Optik, **100**, 107-108 (1995).
23. J. H. Hannay, "Fresnel diffraction as an aperture edge integral," J. Mod. Opt. **47**, 121-124 (2000).
24. Y. Z. Umul, "Uniform boundary diffraction wave theory of Rubinowicz," J. Opt. Soc. Am. A. **27**, 1613-1619 (2010).
25. R. Borghi, "Uniform asymptotics of paraxial boundary diffraction wave," J. Opt. Soc. Am. A. **32**, 685-696 (2015).
26. S. Anokhov, "On problem of the rigorous diffraction quantitative description," Semicon. Phys. Quant. Elect. Optoelec. **2**, 66-69 (1999).
27. R. Kumar, S. K. Kaura, A. K. Sharma, D. P. Chhachhia, and A. K. Aggarwal, "Knife-edge diffraction as an interference phenomenon: an experimental reality", Opt. Laser Tech. **39**, 256-261 (2007).